Indian Journal of Pure & Applied Physics
Vol. 64, November 2026, pp. 1202-1215
DOI: 10.56042/ijpap.v64i11.31857

Hall and Ion-Slip Influence on Tri-Hybrid Jeffery Nanofluid Flowing in an Uneven Stenosed Inclined Catheterized Artery with Variable Permeability and Thermal Conductivity

Jyoti Deshwal & Santosh Chaudhary*
Department of Mathematics, Malaviya National Institute of Technology, Jaipur 302017, India

Received: 22nd May 2026; accepted: 12th October 2026

A rigorous assessment of blood flow behavior in damaged circulatory pathways serves as a cornerstone for improving therapeutic delivery systems and cardiovascular monitoring. This work presents a theoretical characterization of magnetohydrodynamic (MHD) unsteady blood flow within a porous, inclined catheterized arterial system affected by irregular stenosis. To capture the complex rheological behavior of blood, the Jeffery fluid model is employed. Molybdenum disulfide (MoS_2), gold (Au), and magnesium oxide (MgO) nanoparticles are dispersed within blood as the base fluid to develop a tri-hybrid nanofluid. Permeability and thermal conductivity have been considered to be non-constant. This investigation evaluates the influence of Hall and ion-slip currents, Ohmic dissipation, and chemical reaction. To simplify the governing non-linear partial differential equations (PDEs), a coordinate transformation using non-similar variables was employed to derive a dimensionless framework. Under the assumption of mild stenosis, these equations were further refined and solved analytically for velocity, thermal distribution, and concentration using the Homotopy Perturbation Method (HPM). Furthermore, the study quantifies total entropy generation to assess thermodynamic irreversibility. Performance of mono, binary, and ternary hybrid nanofluids is contrasted across various physical parameters to determine their effects on flow, heat and mass transport. Streamline plots are utilized to examine flow behavior. Tri-hybrid configuration outperforms mono and hybrid nanofluids in terms of axial velocity and entropy generation, though it maintains significantly lower thermal and mass concentration profiles. Furthermore, the study suggests that higher Hall and ion-slip coefficients facilitate faster flow while concurrently suppressing thermal distribution. Recirculation is enhanced for variable permeability and Hall parameters. To ensure the reliability of the present model, the findings were validated with existing studies in the field. These findings provide significant insights for the development of nanoparticle-assisted thermal therapies and bio-electromagnetic flow control systems.

Keywords: Hall and ion-slip effects, Inclined catheterized artery, Jeffery fluid model, Tri-hybrid nanofluid, Uneven stenosis, Variable permeability, Variable thermal conductivity

1 Introduction

Hall and ion-slip effects are crucial while considering a strong external magnetic field. Hall parameter is the ratio of the frequencies of electron-cyclotron and electron-atom-collision. The ion-slip effect is generated due to the difference in diffusion velocities of electrons and ions. These effects are worth studying due to their applications in targeted drug delivery systems, magnetic imaging, refrigerator coils, magnetic resonance angiography, etc. The impact of Hall and ion-slip effects on the three-dimensional, steady flow of a second-grade fluidhas been considered[1]. Theoretical solution of the MHD flow equations with ion-slip and Hall effects to establish the asymptotic behavior and well-posedness of the solution[2]. The impact of ion-slip and Hall effects on the peristaltic flow of a viscoelastic fluid through a wall channel with viscous effect and Ohmic heating was demonstrated[3]. The analytic solution for heat transfer in copper-water nanofluid through a horizontal channel with ion-slip and Hall effects has been calculated[4]. The combined impact of thermal radiative flux, ion slip and Hall currents on dusty Casson fluid flowing in a rectangular channel has been examined[5].

Consideration of nanofluids has expanded in recent times due to their exceptional thermal features and applications in medical science. Nanofluids are a mixture of nanometer-sized solid particles (metallic or non-metallic) such as gold (Au),MoS_2, graphene, etc., and the base fluid, like blood, engine oil, water, etc. Nanofluids have vast implications in nuclear reactors, microelectronics, blood diagnosis, nano-medicine, cancer treatment, etc. The phenomenon of

*Corresponding author: E-mail:d11.santosh@yahoo.com

nanotechnology was first established[6]. A hybrid nanofluid consists of two different nanoparticles dispersed in a base fluid, whereas a tri-hybrid nanofluid incorporates three. Such advanced fluids generally exhibit superior thermal and rheological properties compared to conventional nanofluids. The effectiveness of an induced magnetic field on hybrid titanium oxide-copper/water nanofluid flow over a stretchable sheet around a stagnation point has been noticed[7]. The entropy generation analysis of tri-hybrid Maxwell nanofluid flowing through a Riga plate with a heat source and thermal effects wasrecorded[8]. Investigation on how Soret and Dufour influence slip behavior of a tri-hybrid Carreau nanofluid in the stenosed artery was performed[9]. The mixed convective boundary layer flow of ternary hybrid Casson nanofluid with thermal radiation and slip velocity has been investigated[10].

Non-Newtonian fluid models have attracted much attention due to their complex rheological characteristics. The shear rate in such fluid models is directly related to the deformation rate. The Jeffery fluid model is one such model used in modelling various biological and industrial processes. The Jeffery fluids are viscoelastic, that is, they respond to stress. These fluids exhibit both shear-thickening and shear-thinning tendencies, such as shown by milk, blood, ketchup, etc. The influence of relaxation and retardation times is a key consideration of this model. The analytical study of Jeffery nanofluid flow in an asymmetric microchannel under magnetic, electric, and thermal effects was recorded[11]. The influence of the Cattaneo-Christov heat flux model on MHD convective flow of Jeffery fluid past a stretching cylinder was characterized[12]. The multi-membrane pumping process for the biothermal pumping flow of Jeffery fluid in a finite length vertical microchannel with electro-osmosis was introduced[13]. The dynamics of Hall current and radiative heat in Jeffery fluid flowing over a porous stretching surface with convective boundary condition and Ohmic dissipation were described[14]. An analytical study on the impact of heat generation and thermal ray on the slip flow of Jeffery fluid past a wavy porous curved channel was performed[15].

Porous media is a material having a solid frame associated with pores. Variable permeability means the void fraction differs spatially within the medium. Heat transfer can be significantly impacted by variable porosity. Fluid movement is more prominent in areas with higher porosity since there is less resistance there, which leads to higher rates of convective heat transfer. The porous medium's heat distribution is not uniform as a result of variable permeability. Additionally, varying porosity generates transient effects, alters thermal properties and flow patterns. These impacts are important for optimizing the performance and design of systems like underground heat storage, medical devices, electronic devices, etc. The impacts of Navier slip and convective boundary condition on the copper-water nanofluid flow past an inclined channel with variable permeability have been recorded[16]. The constant and variable permeability models, by introducing two conformable spatial derivatives for the classical steady one-dimensional Navier-Stokes model, were compared[17]. A non-similar study of the radiative nanofluid flow over a vertical stretching sheet with inclined magnetic field, variable permeability and viscous heating was performed[18]. The blood flow incorporated with the Casson fluid model over a bi-directional stretching sheet with variable porosity and convective heating has been demonstrated[19]. The impacts of variable permeability and partial slip on blood flowing in a constricted artery with an external magnetic field have been scrutinized[20].

The ability of a material to transfer heat in response to various conditions, such as pressure, temperature, electric field, etc., is called variable thermal conductivity. The majority of the existing research makes the assumption that the fluid's thermophysical characteristics remain constant. Nevertheless, these properties, particularly the thermal conductivity, may change with temperature. This consideration has numerous implications in engineering, biomedicine, industries, etc. The slip flow of compressible Jeffery fluid flowing in a ciliated channel with variable thermal conductivity, magnetic effects and thermal effects was studied[21]. The photothermal diffusion process in a nanoscale semiconductor material with thermoelasticity and non-constant thermal conductivity was examined[22]. The Green Naghdi-II theory to study the impact of fluctuating thermal conductivity and mechanical load on the medium of photothermoelastic semiconducting has been explored[23]. The impact of non-constant thermal conductivity and dual stratification on heat transport in the tetra-hybrid Casson nanofluid flow on a stretchable sheet was described[24]. The Caputo fractional derivatives to study the consequences of fractional Joule heating, variable thermal conductivity and thermal-electrical coupling on MHD flow of a

fractional Oldroyd–B fluid through parallel plates were defined[25].

A catheter is a long, flexible and thin tube mostly made with plasticizer-based PVC materials. Catheters are often used for the diagnosis and treatment of diseased arteries. In balloon angioplasty, catheters are frequently used to clear tiny blockages brought on by atherosclerosis. The catheter is inserted cautiously into a stenotic artery and then inflated to expand the constricted area and dissolve the fat. Blood arteries have been considered to have a zero inclination with the horizontal in the majority of the available research. Nowadays, researchers investigate blood flow in arteries having an inclination, given the well-established fact that ducts within the human body are angled. The pulsatile slip inclined arterial flow of blood with catheterization and magnetic effect has been scrutinized[26]. The power-law fluid model to study the hydro-magnetic blood flowing in a tilted catheterized artery with overlapping stenosis was utilized[27]. The effectiveness of aneurysm and stenosis on the hybrid nanofluidflow in a tapered catheterized inclined artery was considered[28]. The impact of the magnetic field and thermal radiation on the tri-hybrid nanofluid flow in a catheterized inclined artery was observed[29].

The majority of heart diseases are brought on by cellular waste products, accumulation of fatty substances, cholesterol, or plaque development in the artery lumen. This type of plaque buildup in the arteries prevents the flow of blood, and this condition is termed stenosis. Uneven stenosis is the result of the uneven distribution of these fatty materials. Unusual blood flow caused by the squeezed artery leads to irregular coagulation and outflow. The discrete and single-phase models to study the transport properties of Au-blood nanofluid flowing in an irregular stenosed artery with magnetic effects were utilized[30]. An asymptotic study of fluid flow modelled with chemical reaction and the Casson model in a multi-irregular stenosed artery has been performed[31]. The consequences of Lorentz force and varying viscosity on the biomagnetic flow in a tilted,irregular stenosed artery were formulated[32]. A comparative analysis of the Au-blood nanofluid flow incorporated by the Sutterby fluid model in a composite as well as uneven stenosed inclined artery under the body acceleration was reported[33]. The method of finite difference to analyze the impact of an inclined magnetic field on the blood-based nanofluid flowing through a porous uneven/composite stenosed artery was incorporated[34].

The existing literature suggests that the combined impact of Hall and ion-slip currents on the unsteady, slip flow of blood within a tilted, catheterized artery featuring irregular stenosishas not been explored yet. The non-Newtonian characteristics of blood are incorporated using the Jeffery fluid model. MoS_2, Au and MgO are suspended in blood to form the ternary hybrid nanofluid. These nanoparticles were chosen for their proven utility in site-specific drug release, high thermal conductivity, and advanced cancer therapeutics. A variable-permeability model is used to study porosity. Systematic irreversibilities were investigated through the computation of the entropy generation profiles. HPM is employed to calculate the series solution of the system of PDEs. The effectiveness of several governing parameters on fluid flow, entropy, concentration, temperature, and streamline plots is captured through graphs. Computed values for the wall shear rate and the local Sherwood and Nusselt numbers are summarized in the accompanying table.

2 Methods and Materials

This study investigates the unsteady, two-dimensional, and axially symmetric flow of blood through a porous, catheterized artery. The arterial segment, of length L, is characterized by uneven stenosis and is oriented at an angle α. The rheological behavior of the blood is modelled using the Jeffery fluid model. Given the symmetry of the system, a cylindrical coordinate system $(\bar{r}, \bar{\theta}, \bar{z})$ is utilized, where $\bar{r}$and $\bar{z}$indicate radialand axial coordinates and $\bar{\theta}$ denotes tangential coordinate, which is neglected in the present study. Consequently, the velocity is defined by the radial $(\bar{u})$ and axial $(\bar{w})$ components. The electromagnetic field includes a constant magnetic field B_0, incorporating both Hall and ion-slip effects. The flow properties are enhanced by a tri-hybrid nanofluid suspension, consisting of spherical MoS_2, Au, and MgO nanoparticles dispersed in a blood-based medium. The physical configuration is illustrated in Fig. 1.

The Jeffrey fluid model is incorporated using the stress tensor $(\bar{\tau})$

$$\bar{\tau} = \frac{\mu_{th}}{1+\lambda_1}(\dot{\bar{\gamma}} + \lambda_2 \ddot{\bar{\gamma}}) \quad ...(1)$$

where, the subscript th refers to the tri-hybrid nanofluid, μ represents the fluid's viscosity, λ_1 represents the Jeffrey parameter (relaxation time), $\dot{\bar{\gamma}}$ refers to the shear rate and λ_2 is retardation time ratio.

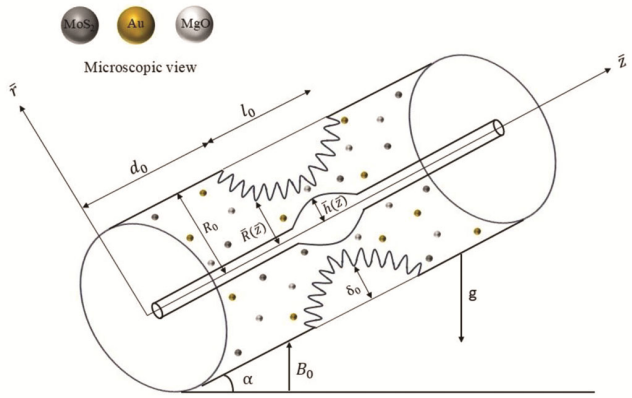

Fig. 1 — Flow geometry

Thegeometric topography of the catheterized artery, incorporating both the uneven stenosis $\bar{R}(\bar{z})$ and the ballooned catheter $\bar{h}(\bar{z})$, is expressed as;

$$\bar{R}(\bar{z}) = \begin{cases} R_0 - 2\delta_0 \begin{cases} \cos\left[\frac{2\pi}{l_0}\left(\frac{\bar{z}-d_0}{2} - \frac{l_0}{4}\right)\right] \\ -\frac{7}{100}\cos\left[\frac{32\pi}{l_0}\left(\bar{z}-d_0-\frac{l_0}{2}\right)\right] \end{cases}, & d_0 \le \bar{z} \le d_0 + l_0 \\ R_0, & \text{otherwise} \end{cases} \quad ...(2)$$

$$\bar{h}(\bar{z}) = \begin{cases} R_0 k^* + \delta_0^* e^{-\pi^2\left(\bar{z}-\bar{z}_d-\frac{1}{2}\right)^2}, & d_0 \le \bar{z} \le d_0 + l_0 \\ R_0 k^*, & \text{otherwise} \end{cases} \quad ...(3)$$

In the above equations, R_0 indicates radius of healthy artery, δ_0, l_0 and $d_0$indicate the depth, length and location of stenosis, $R_0 k^*, \bar{z}_d$ and $\delta_0^*$are the radius, axial displacement and maximum height of the inner tube.

The mathematical framework governing the fluid motion is[4,29]

$$\frac{\partial \overline{u}}{\partial \bar{r}} + \frac{\overline{u}}{\bar{r}} + \frac{\partial \overline{w}}{\partial \bar{z}} = 0 \quad ...(4)$$

$$\rho_{th}\left(\frac{\partial \overline{u}}{\partial \bar{t}} + \overline{u}\frac{\partial \overline{u}}{\partial \bar{r}} + \overline{w}\frac{\partial \overline{u}}{\partial \bar{z}}\right) = -\frac{\partial \overline{p}}{\partial \bar{r}} + \frac{1}{\bar{r}}\frac{\partial}{\partial \bar{r}}(\bar{r}\bar{\tau}_{\bar{r}\bar{r}}) + \frac{\partial}{\partial \bar{z}}(\bar{\tau}_{\bar{r}\bar{z}})$$
$$-\frac{\mu_{th}}{\bar{k}(\bar{r})}\overline{u} + \frac{\sigma_{th}B_0^2}{(1+\beta_e\beta_i)^2+\beta_e^2}[\beta_e\overline{w} - (1+\beta_e\beta_i)\overline{u}]$$
$$+g\left[(\rho\beta_1)_{th}(\overline{T}-T_0) + (\rho\beta_2)_{th}(\overline{C}-C_0)\right]\cos\alpha \quad ...(5)$$

$$\rho_{th}\left(\frac{\partial \overline{w}}{\partial \bar{t}} + \overline{u}\frac{\partial \overline{w}}{\partial \bar{r}} + \overline{w}\frac{\partial \overline{w}}{\partial \bar{z}}\right) = -\frac{\partial \overline{p}}{\partial \bar{z}} + \frac{1}{\bar{r}}\frac{\partial}{\partial \bar{r}}(\bar{r}\bar{\tau}_{\bar{r}\bar{z}}) + \frac{\partial}{\partial \bar{z}}(\bar{\tau}_{\bar{z}\bar{z}})$$
$$-\frac{\mu_{th}}{\bar{k}(\bar{r})}\overline{w} - \frac{\sigma_{th}B_0^2}{(1+\beta_e\beta_i)^2+\beta_e^2}[(1+\beta_e\beta_i)\overline{w} + \beta_e\overline{u}]$$
$$+g\left[(\rho\beta_1)_{th}(\overline{T}-T_0) + (\rho\beta_2)_{th}(\overline{C}-C_0)\right]\sin\alpha \quad ...(6)$$

$$(\rho C_p)_{th}\left(\frac{\partial \overline{T}}{\partial \bar{t}} + \overline{u}\frac{\partial \overline{T}}{\partial \bar{r}} + \overline{w}\frac{\partial \overline{T}}{\partial \bar{z}}\right) = \kappa(\overline{T})\left(\frac{\partial^2 \overline{T}}{\partial \bar{r}^2} + \frac{1}{\bar{r}}\frac{\partial \overline{T}}{\partial \bar{r}} + \frac{\partial^2 \overline{T}}{\partial \bar{z}^2}\right)$$
$$+\frac{\sigma_{th}B_0^2}{(1+\beta_e\beta_i)^2+\beta_e^2}(\overline{u}^2+\overline{w}^2) + Q_0 \quad ...(7)$$

$$\frac{\partial \overline{C}}{\partial \bar{t}} + \overline{u}\frac{\partial \overline{C}}{\partial \bar{r}} + \overline{w}\frac{\partial \overline{C}}{\partial \bar{z}} = D_{th}\left(\frac{\partial^2 \overline{C}}{\partial \bar{r}^2} + \frac{1}{\bar{r}}\frac{\partial \overline{C}}{\partial \bar{r}} + \frac{\partial^2 \overline{C}}{\partial \bar{z}^2}\right) - r_1(\overline{C}-C_0) \quad ...(8)$$

subjected to boundary conditions;

$$\overline{w} = w_c, \overline{T} = T_1, \overline{C} = C_1 \text{at} \bar{r} = \bar{h}(\bar{z})$$
$$\overline{w} = N_1\frac{\partial \overline{w}}{\partial \bar{r}} + N_2\frac{\partial^2 \overline{w}}{\partial \bar{r}^2}, \overline{T} = T_0 - \gamma_t\frac{\partial \overline{T}}{\partial \bar{r}}, \overline{C} = C_0 - \gamma_c\frac{\partial \overline{C}}{\partial \bar{r}} \text{at} \bar{r} = \bar{R}(\bar{z}) \quad ...(9)$$

here, ρ indicates the fluid's density, $\bar{t}$ refers to the time, $\overline{p}$ represents the blood's pressure, $\bar{k}(\bar{r})\left[=\frac{k_0}{1+c\bar{r}}\right]$ represents variable permeability of the surface, k_0 is the constant permeability parameter, c is the variable permeability parameter, σindcates the electrical conductivity, $\beta_e$and β_i are the Hall and ion-slip parameters, g indicates the gravitational acceleration, β_1 and β_2 denotes temperature and concentration dependent coefficients of thermal expansion, $\overline{T}$ represents the system's temperature, C_0 and T_0 refers to the concentration and temperature of stenotic wall, $\overline{C}$ indicates concentration, $\kappa(\overline{T})\left[=\frac{\kappa_{th}}{\lambda(\overline{T}-T_r)}\right]$ is the variable thermal conductivity,κ indicates the thermal conductivity,$T_r\left(=T_0-\frac{1}{\lambda}\right)$ is the reference temperature,λrepresents a constant,C_p represents the specific heat capacitance,Q_0 represents the constant heat source, r_1 refers to chemical reaction rate, D represents the coefficient of mass diffusion,w_c is the catheter velocity, T_1 and C_1 denote temperature and concentration at the center, N_1 and N_2 are the coefficient of first and second order velocity slip, γ_t indicates the coefficient of thermal slip and γ_c denotes the coefficient of concentration slip.

The thermo-physical characteristics of the nanomaterials and the base medium are summarized in Table 1, with the corresponding numerical values presented in Table 2. In this study, the mono-nanofluid is synthesized by suspending MoS_2 particles within the blood. The binary hybrid nanofluid is subsequently formed by introducing Au nanoparticles into the existing MoS_2-blood suspension, while the ternary (tri-hybrid) variant is achieved by adding MgO to the Au-MoS_2-blood mixture. The subscripts

Table1 — Thermo-physical correlations among base fluid, nanofluid, hybrid nanofluid, and tri-hybrid nanofluid

Nanofluid	Hybrid nanofluid	Tri-hybrid nanofluid
$\frac{\mu_{nf}}{\mu_f}=\frac{1}{(1-\varphi_{MoS_2})^{2.5}}$	$\frac{\mu_{hnf}}{\mu_{nf}}=\frac{1}{(1-\varphi_{Au})^{2.5}}$	$\frac{\mu_{th}}{\mu_{hnf}}=\frac{1}{(1-\varphi_{MgO})^{2.5}}$
$\frac{\rho_{nf}}{\rho_f}=1-\varphi_{MoS_2}+\frac{\rho_{MoS_2}}{\rho_f}\varphi_{MoS_2}$	$\frac{\rho_{hnf}}{\rho_{nf}}=1-\varphi_{Au}+\frac{\rho_{Au}}{\rho_{nf}}\varphi_{Au}$	$\frac{\rho_{th}}{\rho_{hnf}}=1-\varphi_{MgO}+\frac{\rho_{MgO}}{\rho_{hnf}}\varphi_{MgO}$
$\frac{\sigma_{nf}}{\sigma_f}=\frac{\sigma_{MoS_2}+2\sigma_f+2(\sigma_{MoS_2}-\sigma_f)\varphi_{MoS_2}}{\sigma_{MoS_2}+2\sigma_f-(\sigma_{MoS_2}-\sigma_f)\varphi_{MoS_2}}$	$\frac{\sigma_{hnf}}{\sigma_{nf}}=\frac{\sigma_{Au}+2\sigma_{nf}+2(\sigma_{Au}-\sigma_{nf})\varphi_{Au}}{\sigma_{Au}+2\sigma_{nf}-(\sigma_{Au}-\sigma_{nf})\varphi_{Au}}$	$\frac{\sigma_{th}}{\sigma_{hnf}}=\frac{\sigma_{MgO}+2\sigma_{hnf}+2(\sigma_{MgO}-\sigma_{hnf})\varphi_{MgO}}{\sigma_{MgO}+2\sigma_{hnf}-(\sigma_{MgO}-\sigma_{hnf})\varphi_{MgO}}$
$\frac{(\rho\beta_r)_{nf}}{(\rho\beta_r)_f}=1-\varphi_{MoS_2}+\frac{(\rho\beta_r)_{MoS_2}}{(\rho\beta_r)_f}\varphi_{MoS_2}$ (here$r=1,2$)	$\frac{(\rho\beta_r)_{hnf}}{(\rho\beta_r)_{nf}}=1-\varphi_{Au}+\frac{(\rho\beta_r)_{Au}}{(\rho\beta_r)_{nf}}\varphi_{Au}$	$\frac{(\rho\beta_r)_{th}}{(\rho\beta_r)_{hnf}}=1-\varphi_{MgO}+\frac{(\rho\beta_r)_{MgO}}{(\rho\beta_r)_{hnf}}\varphi_{MgO}$
$\frac{(\rho C_p)_{nf}}{(\rho C_p)_f}=1-\varphi_{MoS_2}+\frac{(\rho C_p)_{MoS_2}}{(\rho C_p)_f}\varphi_{MoS_2}$	$\frac{(\rho C_p)_{hnf}}{(\rho C_p)_{nf}}=1-\varphi_{Au}+\frac{(\rho C_p)_{Au}}{(\rho C_p)_{nf}}\varphi_{Au}$	$\frac{(\rho C_p)_{th}}{(\rho C_p)_{hnf}}=1-\varphi_{MgO}+\frac{(\rho C_p)_{MgO}}{(\rho C_p)_{hnf}}\varphi_{MgO}$
$\frac{\kappa_{nf}}{\kappa_f}=\frac{\kappa_{MoS_2}+2\kappa_f+2(\kappa_{MoS_2}-\kappa_f)\varphi_{MoS_2}}{\kappa_{MoS_2}+2\kappa_f-(\kappa_{MoS_2}-\kappa_f)\varphi_{MoS_2}}$	$\frac{\kappa_{hnf}}{\kappa_{nf}}=\frac{\kappa_{Au}+2\kappa_{nf}+2(\kappa_{Au}-\kappa_{nf})\varphi_{Au}}{\kappa_{Au}+2\kappa_{nf}-(\kappa_{Au}-\kappa_{nf})\varphi_{Au}}$	$\frac{\kappa_{th}}{\kappa_{hnf}}=\frac{\kappa_{MgO}+2\kappa_{hnf}+2(\kappa_{MgO}-\kappa_{hnf})\varphi_{MgO}}{\kappa_{MgO}+2\kappa_{hnf}-(\kappa_{MgO}-\kappa_{hnf})\varphi_{MgO}}$
$\frac{D_{nf}}{D_f}=(1-\varphi_{MoS_2})^{2.5}$	$\frac{D_{hnf}}{D_{nf}}=(1-\varphi_{Au})^{2.5}$	$\frac{D_{th}}{D_{hnf}}=(1-\varphi_{MgO})^{2.5}$

Table 2 — Values in numbers for the thermophysical characteristics of the base fluid and the nanoparticles

Particles	$\rho(Kg/m^3)$	$\sigma(S/m)$	$\beta(K^{-1}\times10^{-5})$	$C_p(J/KgK)$	$\kappa(W/mK)$
Blood	1050	1.33	0.18	3617	0.52
MoS_2	5060	2.09×10^{-5}	2.8424	397.21	904.4
Au	19300	4.5×10^{7}	1.42	129.1	320
MgO	3580	5.392×10^{-7}	1.31	879	30

f, nf, and hnf represent the base fluid, nanofluid, and hybrid nanofluid, respectively. Furthermore, the volume concentrations for each nanoparticle species are indicated by φ_{MoS_2}, φ_{Au}, and φ_{MgO}.

The primary governing equations are simplified by introducing the dimensionless parameters defined below

$$r=\frac{\bar{r}}{R_0},z=\frac{\bar{z}}{l_0},t=\frac{w_c\bar{t}}{l_0}\ u=\frac{l_0\overline{u}}{\delta_0 w_c},w=\frac{\overline{w}}{w_c},R=\frac{\bar{R}}{R_0},h=\frac{\bar{h}}{R_0},\delta=\frac{\delta_0}{R_0}$$

$$\epsilon=\frac{R_0}{l_0},d=\frac{d_0}{l_0},\delta^*=\frac{\delta_0^*}{R_0},z_d=\frac{2\bar{z}_d+1-l_0}{2l_0},p=\frac{R_0^2}{l_0\mu_f w_c}\overline{p},\boldsymbol{\tau}=\frac{R_0\bar{\boldsymbol{\tau}}}{w_c\mu_f}$$

$$k(r)=\frac{\bar{k}(\bar{r})}{R_0^2},\theta=\frac{T_0-\bar{T}}{T_0-T_1},\Phi=\frac{C_0-\bar{C}}{C_0-C_1}\ \#\qquad ...(10)$$

here, u and w signify the dimensionless velocity fields in the non-dimensional radial (r) and axial (z) directions, respectively, t denotes the non-dimensional time, R indicates the non-dimensional radius of stenotic artery, h denotes dimensionless radius of catheter, δ refers to the stenosis depth parameter, d refers to dimensionless stenosis location, ϵ denotes wave number, δ^* is the dimensionless maximum height of the catheter, z_d is the dimensionless axial displacement of the catheter, p denotes non-dimensional pressure, τ indicates dimensionless stress tensor, $k(r)$ is the dimensionless variable permeability, θ and Φ denote dimensionless temperature and concentration.

The following scaling assumptions, $\epsilon=O(1)$ along with$\delta\ll1$, are applied to the model, indicating that wave number is of order one while the stenosis height is localized. Consequently, the dimensionless Eqs. (4)-(9) are transformed into;

$$\frac{\partial w}{\partial z}=0 \qquad ...(11)$$

$$\frac{\partial p}{\partial r}=0 \qquad ...(12)$$

$$\frac{\partial p}{\partial z}=\frac{\mu_{th}}{\mu_f}\frac{1}{1+\lambda_1}\frac{1}{r}\frac{\partial}{\partial r}\left(r\frac{\partial w}{\partial r}\right)-\frac{\mu_{th}}{\mu_f}\frac{1}{k(r)}w-\frac{\sigma_{th}}{\sigma_f}\frac{M(1+\beta_e\beta_i)}{(1+\beta_e\beta_i)^2+\beta_e^2}w+\left[\frac{(\rho\beta_1)_{th}}{(\rho\beta_1)_f}Gr\theta+\frac{(\rho\beta_2)_{th}}{(\rho\beta_2)_f}Gc\Phi\right]\sin\alpha^{\#} \qquad ...(13)$$

$$\frac{\kappa_{th}}{\kappa_f}\theta_t\left(\frac{\partial^2\theta}{\partial r^2}+\frac{1}{r}\frac{\partial\theta}{\partial r}\right)+\frac{\sigma_{th}}{\sigma_f}\frac{MPrEc}{(1+\beta_e\beta_i)^2+\beta_e^2}w^2(\theta_t-\theta)+S(\theta_t-\theta)=0 \qquad ...(14)$$

$$\frac{D_{th}}{D_f}\left(\frac{\partial^2\Phi}{\partial r^2}+\frac{1}{r}\frac{\partial\Phi}{\partial r}\right)-Sc\phi\Phi=0 \qquad ...(15)$$

the corresponding boundary coditions are defined as;

$$w = 1, \theta = 1, \Phi = 1 \text{at } r = h(z)$$
$$w = -\gamma_1 \frac{\partial w}{\partial r} - \gamma_2 \frac{\partial^2 w}{\partial r^2}, \theta = -\gamma_3 \frac{\partial \theta}{\partial r}, \Phi = -\gamma_4 \frac{\partial \Phi}{\partial r} \text{at } r = R(z) \quad ...(16)$$

where, $M\left(=\frac{\sigma_f B_0^2 R_0^2}{\mu_f}\right)$ is magnetic number, $Gr\left[=\frac{g(\rho\beta_1)_f R_0^2 (T_1 - T_0)}{w_c \mu_f}\right]$ denotes Grashof number, $Gc\left[=\frac{g(\rho\beta_2)_f R_0^2 (C_1 - C_0)}{w_c \mu_f}\right]$ is solutal Grashof number, $\theta_t\left[=-\frac{1}{\lambda(T_1 - T_0)}\right]$ is thermal conductivity parameter, $Pr\left[=\frac{\mu_f (C_p)_f}{\kappa_f}\right]$ represents the Prandtl number, $Ec\left[=\frac{w_c^2}{(C_p)_f (T_1 - T_0)}\right]$ is Eckert number, $S = \left[\frac{Q_0 R_0^2}{\kappa_f (T_1 - T_0)}\right]$ is heat source parameter, $Sc\left(=\frac{\mu_f}{\rho_f D_f}\right)$ is Schmidt number, $\phi\left(=\frac{\rho_f r_1 R_0^2}{\mu_f}\right)$ is chemical reaction parameter, $\gamma_1\left(=-\frac{N_1}{R_0}\right)$and $\gamma_2\left(=-\frac{N_2}{R_0^2}\right)$ are first and second order velocity slip parameters, $\gamma_3\left(=\frac{\gamma_t}{R_0}\right)$ denotes parameter for thermal slip, $\gamma_4\left(=\frac{\gamma_c}{R_0}\right)$ represents concentration slip parameter;

$$h(z) = \begin{cases} k^* + \delta^* e^{-\pi^2 l_0^2 \left(z - z_d - \frac{1}{2}\right)^2}, & d \le z \le d+1 \text{ and} \\ k^*, & \text{otherwise} \end{cases}$$

$$R(z) = \begin{cases} 1 - 2\delta\left\{\cos\left[\pi\left(z - d - \frac{1}{2}\right)\right] - \frac{7}{100}\cos[16\pi(2(z-d)-1)]\right\}, & d \le z \le d+1 \\ 1, & \text{otherwise} \end{cases}$$

The physical characteristics of the flow, heat, and mass transfer are quantified through the skin friction (C_f), Sherwood number (Sh), and Nusselt number (Nu) which are characterized by;

$$C_f = \frac{\bar{\tau}_{\bar{r}\bar{z}}}{\rho_f w_c^2/2}\Big|_{\bar{r}=\bar{R}(\bar{z})}, Nu = \frac{R_0}{\kappa_f (T_1 - T_0)}\left(-\kappa(\bar{T})\frac{\partial \bar{T}}{\partial \bar{r}}\right)\Big|_{\bar{r}=\bar{R}(\bar{z})},$$
$$Sh = \frac{R_0}{D_f (C_1 - C_0)}\left(-D_{th}\frac{\partial \bar{C}}{\partial \bar{r}}\right)\Big|_{\bar{r}=\bar{R}(\bar{z})} \quad ...(17)$$

Substitute Eq. (10) in Eq. (17) to get;

$$ReC_f = \frac{2\mu_{th}}{\mu_f}\frac{1}{1+\lambda_1}\frac{\partial w}{\partial r}\Big|_{r=R(z)}, Nu = -\frac{\kappa_{th}}{\kappa_f}\frac{\theta_t}{\theta_t - \theta}\frac{\partial \theta}{\partial r}\Big|_{r=R(z)}, Sh = -\frac{D_{th}}{D_f}\frac{\partial \Phi}{\partial r}\Big|_{r=R(z)} \quad ...(18)$$

where, $Re\left(=\frac{\rho_f w_c R_0}{\mu_f}\right)$ denotes Reynolds number.

2.1 Entropy Analysis

To evaluate the irreversibility within the ternary hybrid nanofluid system, the entropy generation rate (S_{gen}) is formulated as follows

$$S_{gen} = \frac{\kappa(\bar{T})}{T_1^2}\left[\left(\frac{\partial \bar{T}}{\partial \bar{r}}\right)^2 + \left(\frac{\partial \bar{T}}{\partial \bar{z}}\right)^2\right] + \frac{\mu_{th}}{T_1 \bar{k}(\bar{r})}\bar{w}^2 + \frac{\sigma_{th}}{T_1}\frac{B_0^2}{(1+\beta_e\beta_i)^2 + \beta_e^2}(\bar{u}^2 + \bar{w}^2) \quad ...(19)$$

Non-dimensional expression for entropy generation is found by substituting Eq. (10) in Eq. (19)

$$N_G = \frac{\kappa_{th}}{\kappa_f}\frac{\theta_t}{\theta_t - \theta}\left(\frac{\partial \theta}{\partial r}\right)^2 + \frac{\mu_{th}}{\mu_f}\frac{PrEc}{\omega_t k(r)}w^2 + \frac{\sigma_{th}}{\sigma_f}\frac{MPrEc}{\omega_t[(1+\beta_e\beta_i)^2 + \beta_e^2]}w^2 \quad ...(20)$$

where, $N_G\left[=\frac{T_1^2 R_0^2}{\kappa_f (T_1 - T_0)^2}S_{gen}\right]$ is entropy rate and $\omega_t\left(=\frac{T_1 - T_0}{T_1}\right)$ is temperature proportion.

2.2 Solution Methodology

The HPM is an analytical technique for addressing linear and nonlinear PDEs. In HPM, an equation is converted into a homotopy that continuously transitions from a straightforward problem to the original intricate problem. The advantages encompass simplicity and efficiency in solution provision, flexibility in managing substantial perturbations, applicability to a diverse array of PDEs, and swift convergence to precise solutions.

Eqs. (13)-(15) are reformulated as;

$$\frac{1}{r}\frac{\partial}{\partial r}\left(r\frac{\partial w}{\partial r}\right) - \frac{a_0}{k(r)}w - a_1 w + a_2\theta + a_3\Phi - a_4 = 0 \quad ...(21)$$

$$\frac{1}{r}\frac{\partial}{\partial r}\left(r\frac{\partial \theta}{\partial r}\right) + a_5 + a_6 w^2 - (a_7 + a_8 w^2)\theta = 0 \quad ...(22)$$

$$\frac{1}{r}\frac{\partial}{\partial r}\left(r\frac{\partial \Phi}{\partial r}\right) - a_9\Phi = 0 \quad ...(23)$$

In the above equations, $a_0 = 1 + \lambda_1$, $a_1 = \frac{\mu_f}{\mu_{th}}\frac{\sigma_{th}}{\sigma_f}\frac{a_0 M(1+\beta_e\beta_i)}{(1+\beta_e\beta_i)^2+\beta_e^2}$, $a_2 = \frac{\mu_f}{\mu_{th}}\frac{(\rho\beta_1)_{th}}{(\rho\beta_1)_f}a_0 Gr\sin\alpha$, $a_3 = \frac{\mu_f}{\mu_{th}}\frac{(\rho\beta_2)_{th}}{(\rho\beta_2)_f}a_0 Gc\sin\alpha$, $a_4 = \frac{\mu_f}{\mu_{th}}a_0\frac{\partial p}{\partial z}$, $a_5 = \frac{\kappa_f}{\kappa_{th}}S$, $a_6 = \frac{\sigma_{th}}{\sigma_f}\frac{\kappa_f}{\kappa_{th}}\frac{MPrEc}{(1+\beta_e\beta_i)^2+\beta_e^2}$, $a_7 = \frac{a_5}{\theta_t}$, $a_8 = \frac{a_6}{\theta_t}$, and $a_9 = \frac{D_f}{D_{th}}Sc\phi$.

To resolve the aforementioned differential Eqs. (21)-(23), a Homotopy must be established on a domain $\mathcal{D}$ having a minor perturbation parameter

$(\bar{q} \in [0,1])$. The homotopies $w(r,\bar{q}), \theta(r,\bar{q}), \Phi(r,\bar{q}): \mathcal{D} \times [0,1] \to \mathbb{R}$ are defined by

$$H(w,\bar{q}) = (1-\bar{q})[L(w) - L(w_0)] + \bar{q}[L(w) - \frac{a_0}{k(r)}w - a_1 w + a_2\theta + a_3\Phi - a_4] = 0 \quad ...(24)$$

$$H(\theta,\bar{q}) = (1-\bar{q})[L(\theta) - L(\theta_0)] + \bar{q}\left[\begin{matrix}L(\theta) + a_5 + a_6 w^2 - \\ (a_7 + a_8 w^2)\theta\end{matrix}\right] = 0 \quad ...(25)$$

$$H(\Phi,\bar{q}) = (1-\bar{q})[L(\Phi) - L(\Phi_0)] + \bar{q}[L(\Phi) - a_9\Phi] = 0 \quad ...(26)$$

here, $L\left[=\frac{1}{r}\frac{\partial}{\partial r}\left(r\frac{\partial}{\partial r}\right)\right]$ refers to differential operator while w_0, θ_0, Φ_0 are initial guesses that are taken as $w_0 = 1 - \frac{r^2-h^2}{R^2-h^2+2\gamma_1 R+2\gamma_2}, \theta_0 = 1 - \frac{r-h}{R-h+\gamma_3}$, and $\Phi_0 = 1 - \frac{r-h}{R-h+\gamma_4}$.

The analytical forms of the solutions to Eqs. (24)-(26) are given as

$$w = \sum_{i=0}^{\infty} \bar{q}^i w_i \quad ...(27)$$

$$\theta = \sum_{i=0}^{\infty} \bar{q}^i \theta_i \# \quad ...(28)$$

$$\Phi = \sum_{i=0}^{\infty} \bar{q}^i \Phi_i \# \quad ...(29)$$

For $\bar{q} \to 1$, the preceding equations are reduced to

$$w(r,z) = \sum_{i=0}^{\infty} w_i \quad ...(30)$$

$$\theta(r,z) = \sum_{i=0}^{\infty} \theta_i \quad ...(31)$$

$$\Phi(r,z) = \sum_{i=0}^{\infty} \Phi_i \quad ...(32)$$

After several computations, the fluidic velocity, temperature, and concentrations' approximate condensed form solution are computed as

$$w(r,z) = A_0 + A_1 r^2 + A_2 r^3 + A_3 r^4 + A_4 r^5 + A_5 \log r \quad ...(33)$$

$$\theta(r,z) = A_6 + A_7 r + A_8 r^2 + A_9 r^3 + A_{10} r^4 + A_{11} r^5 + A_{12} r^6 + A_{13} r^7 + A_{14} \log r \quad ...(34)$$

$$\Phi(r,z) = A_{15} + A_{16} r + A_{17} r^2 + A_{18} r^3 + A_{19} r^4 + A_{20} \log r + A_{21} r \log r + A_{22} r^2 \log r + A_{23} r^3 \log r + A_{24} r^4 \log r \quad ...(35)$$

where, $A_i (i = 0,1,,24)$ are constants.

The expression used to get the analogous stream function (ψ) is $w = \frac{1}{r}\frac{\partial \psi}{\partial r}$ with $\psi = 0$ at $r = h$ and it is computed as

$$\psi(r,z) = \frac{1}{2}A_0(r^2-h^2) + \frac{1}{4}A_1(r^4-h^4) + \frac{1}{5}A_2(r^5-h^5) + \frac{1}{6}A_3(r^6-h^6) + \frac{1}{7}A_4(r^7-h^7) + \frac{1}{4}A_5[2(r^2 \log r - h^2 \log h) - (r^2-h^2)] \quad ...(36)$$

3 Results and Discussion

The primary focus of this section is to analyze the effects of key governing parameters on the velocity (w), concentration (Φ), temperature (θ), entropy rate (N_G) and streamlines via tables and graphs. Specifically, the impacts of the Jeffrey parameter $(\lambda_1 \in [0,0.4])$, variable permeability parameter, $(c \in [5,25])$, Hall parameter $(\beta_e \in [0,1])$, ion-slip parameter $(\beta_i \in [0,1])$, the inclination angle of the artery $\left(\alpha \in \left[0,\frac{\pi}{2}\right]\right)$, thermal conductivity parameter $(\theta_t \in [-10,-2])$, Eckert number $(Ec \in [1,3])$, chemical reaction parameter $(\phi \in [1,9])$, thermal slip parameter $(\gamma_3 \in [0,0.2])$ and concentration slip parameter $(\gamma_4 \in [0.1,0.9])$ are provided in Figs. 2-16. The assignedvalues of critical parameters are $\lambda_1 =$

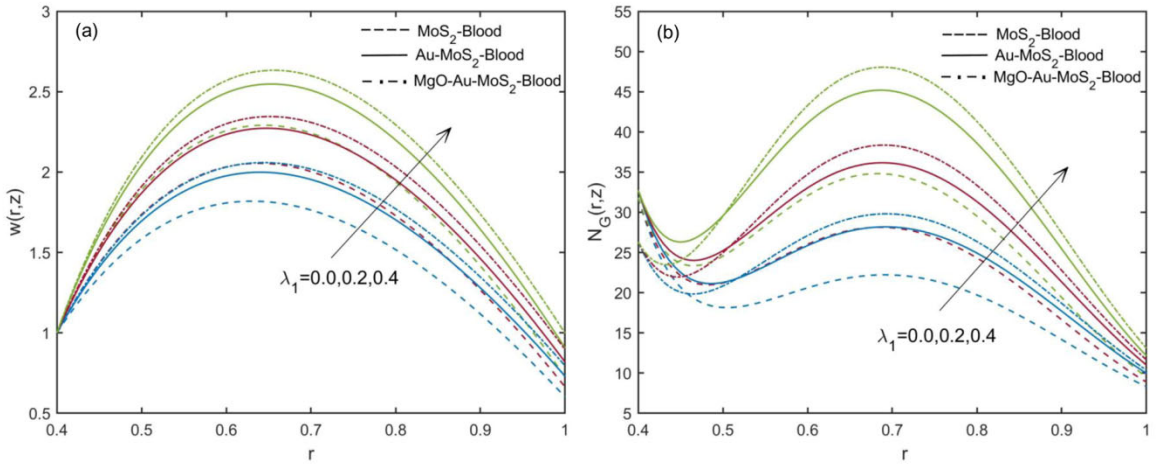

Fig. 2 — Deviations in (a) w(r, z);and (b) $N_G(r,z)$ against λ_1

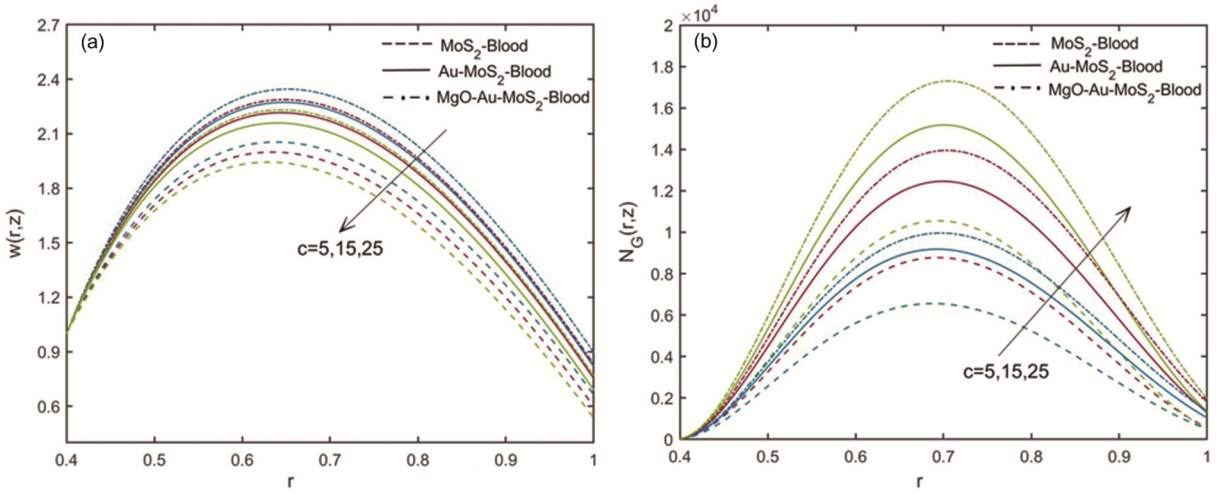

Fig. 3 — Deviations in (a) $w(r,z)$; and (b) $N_G(r,z)$ against c

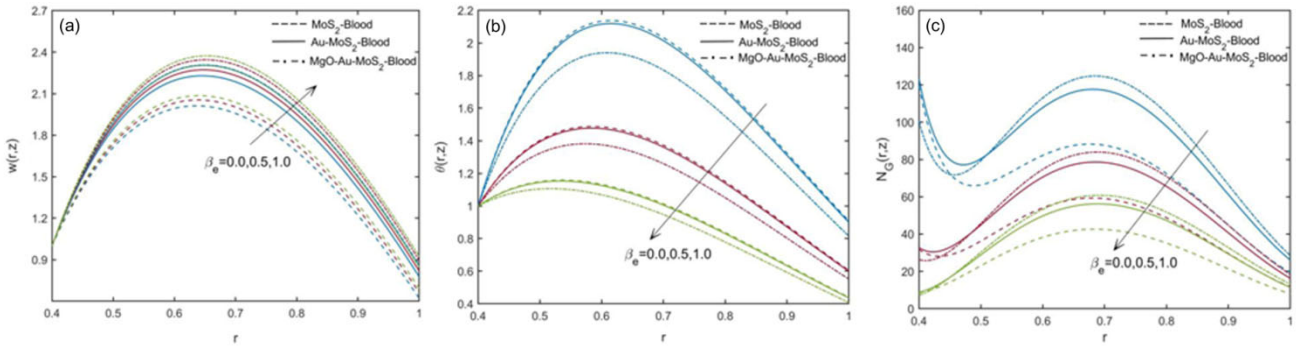

Fig. 4 — Deviations in (a) $w(r,z)$, (b) $\theta(r,z)$; and (c) $N_G(r,z)$ against β_e

$0.2, k_0 = 10, c = 5, M = 2, \beta_e = 0.5, \beta_i = 0.5, Gr = 5, Gc = 5, \alpha = \frac{\pi}{4}, Pr = 21, Ec = 1, S = 0.5, Sc = 1, \phi = 5, \gamma_1 = 0.1, \gamma_2 = -0.2, \gamma_3 = 0.1, \gamma_4 = 0.1, \omega_t = 5, k^* = 0.4, \delta^* = 0.2, l_0 = 1, z = 2, z_d = 0.2, \delta = 1, d = 2, \varphi_{MoS_2} = 0.01, \varphi_{Au} = 0.02$ and $\varphi_{MgO} = 0.03$.

Figure 2 (a) and (b) demonstrate the impact of the Jeffrey parameter (λ_1) on axial velocity and entropy. Entropy rate and axial velocity enhance with rising values of λ_1. The Jeffrey parameter is the ratio of relaxation to retardation time, and $\lambda_1 < 1$ indicates that relaxation time is shorter than retardation time. Due to this, fluid recovery is faster under stress, escalating the flow velocity and entropy.

The influence of the permeability factor (c) on the fluidic and thermodynamic behavior is depicted in Fig. 3 (a) and (b). A clear inverse relationship is observed: as c increases, the axial flow velocity diminishes due to the enhanced drag forces exerted by the porous medium. This restriction in flow is accompanied by a concurrent rise in total entropy generation, reflecting greater irreversibility in the system.

Figures 4(a)-(c) and 5(a)-(c) depict the consequences of Hall parameter (β_e) and ion-slip parameter (β_i) on fluidic, thermal and entropy rate. Entropy rate and temperature decline while the flow velocity enhances for increased values of β_e and β_i. Hall and ion-slip currents arise due to the interaction between the imposed magnetic field and the motion of charged ions present in the blood. The fluid is pushed in the direction of the flow and the spatial distribution of Ohmic heating alters with rising values of β_e and β_i, which results in escalated flow velocity and reduced entropy and thermal rates.

Effectiveness of the artery's inclination angle (α) on fluid velocity and entropy are illustrated in Fig. 6 (a) and (b). An increase in α leads to higher axial velocity and entropy generation. This is attributed to the enhancement of the gravitational component along the axial direction with rising α, which facilitates

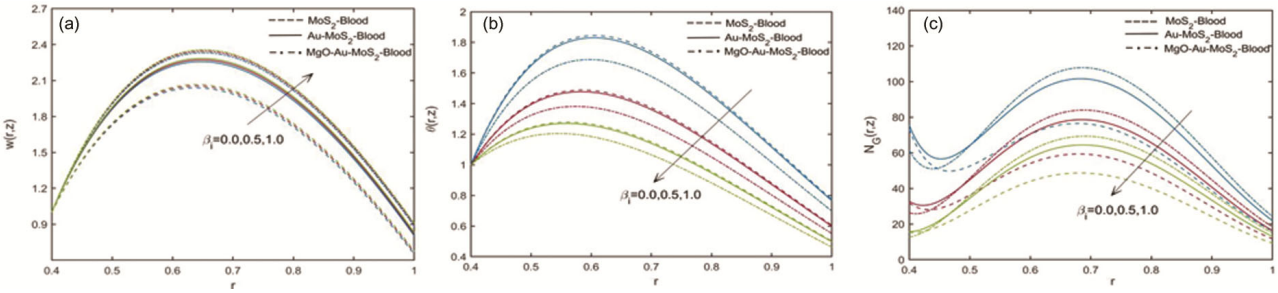

Fig. 5 — Deviations in (a) $w(r,z)$, (b) $\theta(r,z)$; and (c) $N_G(r,z)$ against β_i

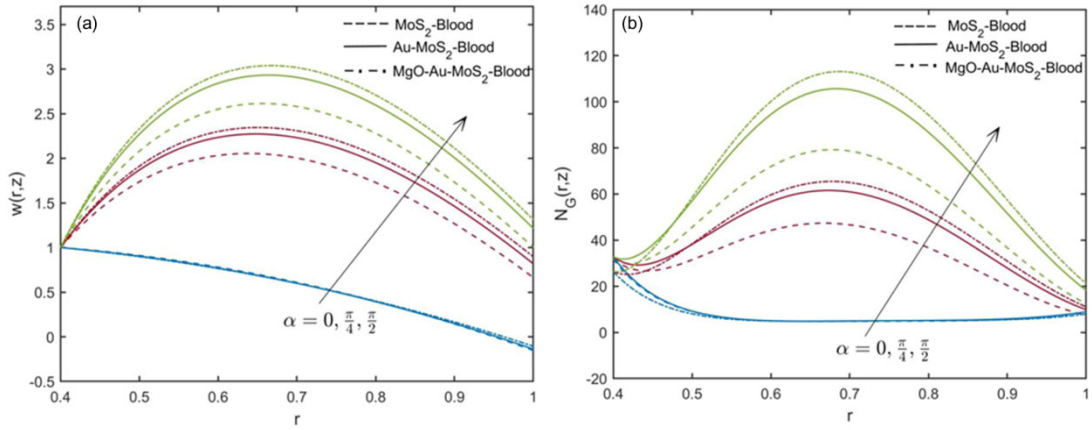

Fig. 6 — Deviations in (a) $w(r,z)$; and (b) $N_G(r,z)$ against α

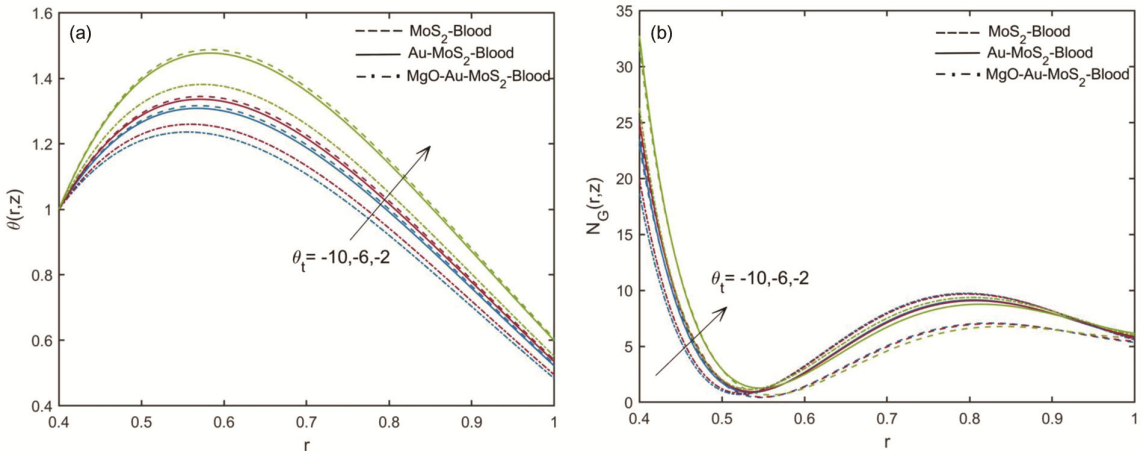

Fig. 7 — Deviations in (a) $\theta(r,z)$; and (b) $N_G(r,z)$ against θ_t

blood flow and consequently elevates both entropy and velocity.

Figure 7 (a) and (b) depict the consequence of the thermal conductivity parameter (θ_t) on thermal and entropy profiles. There is a boost in temperature with a hype in θ_t, whereas entropy shows a non-monotonic behavior. An increase in $\theta_t$enhances the nanofluid's microscopic heat diffusion by reducing thermal resistance, which accelerates thermal transport across fluid layers, expands the thermal boundary layer, and uniformly elevates the temperature and entropy rate.

The temperature and entropy profiles with the Eckert number (Ec) given in Figs. 8(a) and (b). As Ec scales upward, there is a noticeable enhancement in the thermal and entropy profiles. Physically, higher values of Ec signifies a dominant role of Ohmic and viscous heating within the boundary layer. This surplus of heat not only elevates the fluid temperature

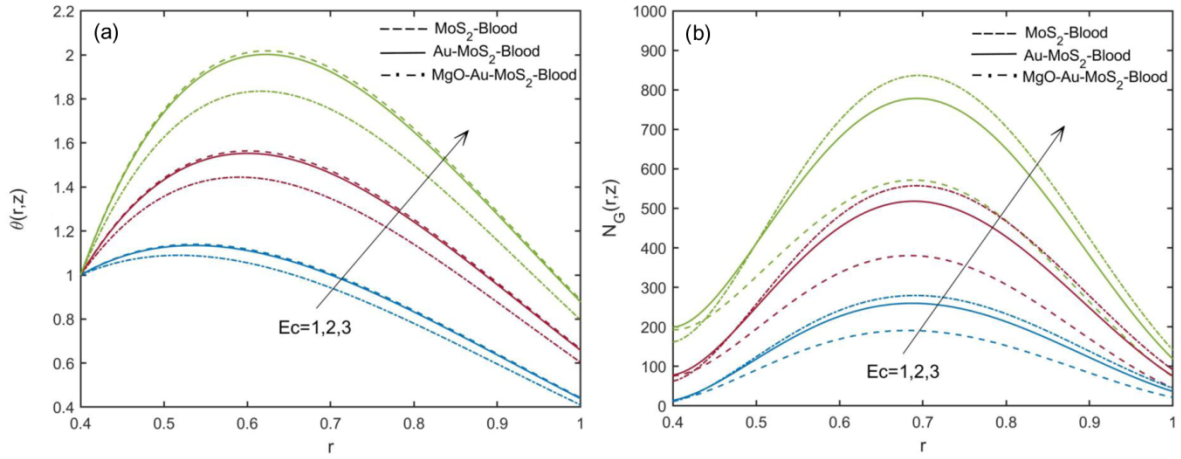

Fig. 8 — Deviations in (a) $\theta(r,z)$; and (b) $N_G(r,z)$ against Ec

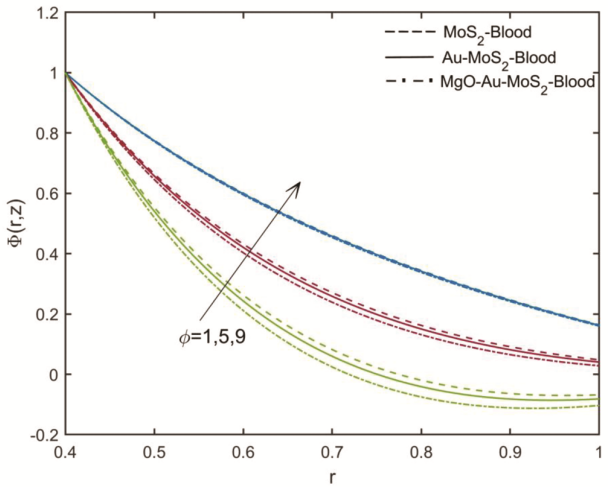

Fig. 9 — Deviations in $\Phi(r,z)$against ϕ

but also accelerates the entropy generation rate due to increased molecular disorder.

Figure 9 depicts the variations in the concentration profiles against the chemical reaction parameter (ϕ). The concentration rises with increased values of ϕ. An increase in ϕ accelerates the rate of species generation per unit volume through a constructive chemical reaction, which enhances molecular species transportation and elevates the concentration profile.

The axial flow field, thermal state, and entropy production are plotted against the thermal slip parameter (γ_3) in Fig. 10(a)-(c). The flow velocity diminishes with a rise in γ_3 while temperature enhances. There is a reduced entropy rate near the catheter wall with hype in γ_3, but it starts to boost near the arterial wall. The hype in γ_3 results in increased retained internal thermal energy in the system, resulting in rising temperature and entropy.

Figure 11(a)-(c) reflect the influence of concentration slip parameter (γ_4) on flow velocity, concentration and entropy profiles. Axial velocity, concentration and entropy de-escalate with a boost in γ_4. The mass flux across the wall reduces with enhanced γ_4, which decreases the axial velocity, entropy and concentration.

Figures 12(a)-(c) and 13(a)-(c) demonstrate the trapping phenomenon for λ_1 and c. As the Jeffrey fluid parameter (λ_1) increases, a notable contraction in the bolus trapping zone is observed. This occurs because the enhancement of λ_1 signifies a shift where elastic forces dominate over viscous effects, effectively suppressing the formation of recirculation eddies. In contrast, the permeability parameter (c) exhibits the opposite effect; as c rises, the intensified porous resistance disrupts the streamlined flow, leading to more pronounced flow instabilities and an expansion of the trapping regions.

The streamline distributions illustrating the influence of the β_e and β_i are presented in Figs. 14(a)-(c) and 15(a)-(c)Trapping enhances with a rise in β_e, and the opposite is true for β_i. The cross-flow motion escalates with a boost in β_e, resulting in prominent recirculation zones. There is a reduced Lorentz drag with increasing β_i, which weakens the trapping phenomenon.

Figures 16(a)-(c) show the streamlined plots for α. The recirculation zone becomes less prominent with rising values of α. As the artery moves from being horizontal to vertical, the gravitational force acts more strongly, resulting in less compact recirculation zones.

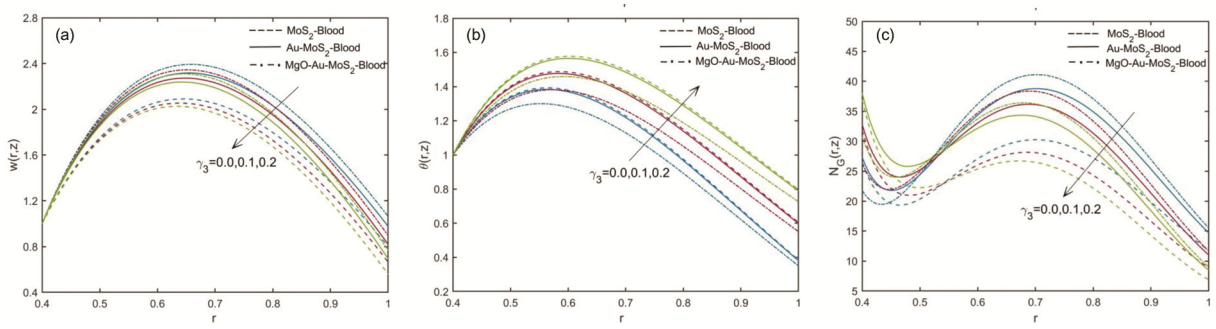

Fig. 10 — Deviations in (a) $w(r,z)$, (b) $\theta(r,z)$; and (c) $N_G(r,z)$ against γ_3

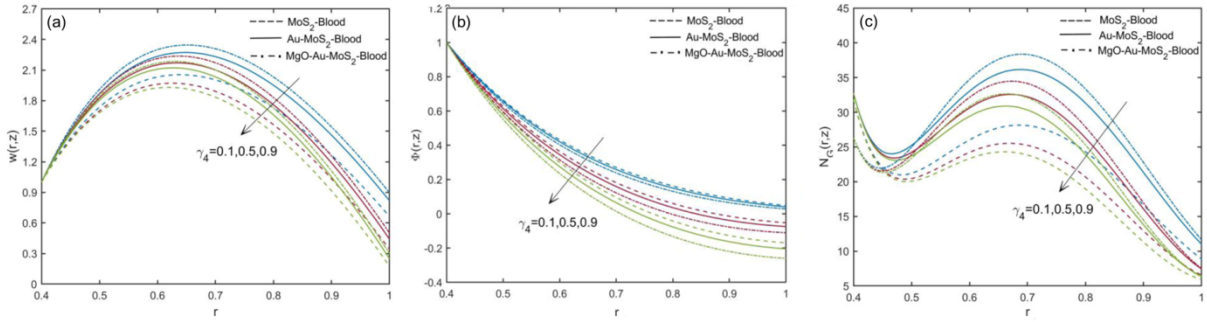

Fig. 11 — Deviations in (a) $w(r,z)$, (b) $\Phi(r,z)$; and (c) $N_G(r,z)$ against γ_4

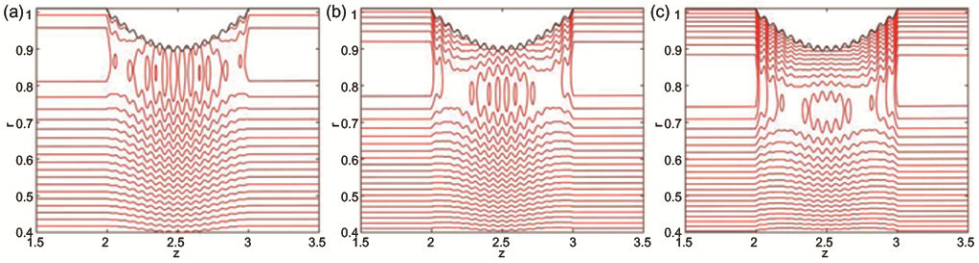

Fig. 12 — Streamlines for (a) $\lambda_1 = 0.0$, (b) $\lambda_1 = 0.2$; and (c) $\lambda_1 = 0.4$

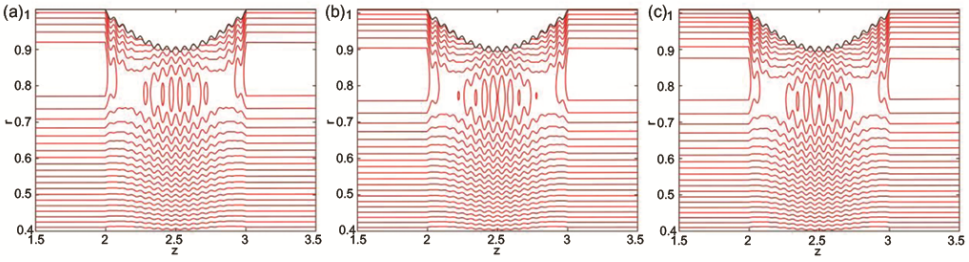

Fig. 13 — Streamlines for (a) $c = 5$, (b) $c = 15$; and (c) $c = 25$

Table 3 illustrates the comparative variations in the local skin friction coefficient, Nusselt number, and Sherwood number across the mono, di, and tri-hybrid nanofluid models. According to Eq. (18), the magnitudes of wall shear stress, thermal transport, andmass flux are indirect relationwith the radial gradients of velocity$\left(\frac{\partial w}{\partial r}\right)_{r=1}$, temperature $\left(\frac{\partial \theta}{\partial r}\right)_{r=1}$, and concentration $\left(\frac{\partial \Phi}{\partial r}\right)_{r=1}$, respectively. A reduction in skin friction coefficient is observed with enhancedvalues of$\lambda_1, \beta_e, \beta_i, \alpha, \gamma_3$ and γ_4, while the opposite is observed for c for all three nanofluids. The

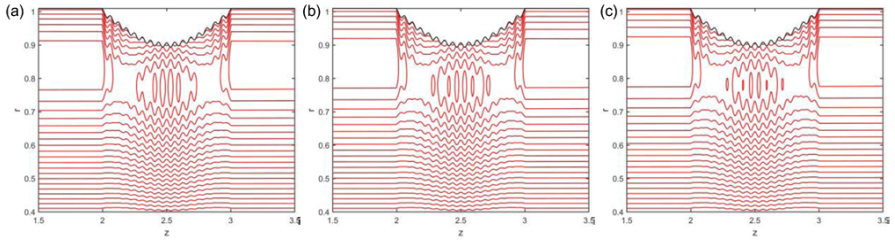

Fig. 14 — Streamlines for (a) $\beta_e = 0.0$, (b) $\beta_e = 0.5$; and (c) $\beta_e = 1.0$

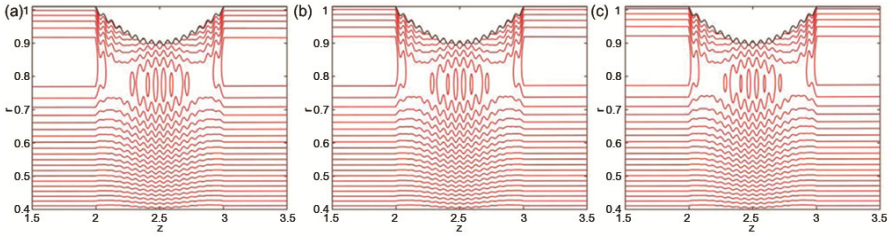

Fig. 15 — Streamlines for (a) $\beta_i = 0.0$, (b) $\beta_i = 0.5$; and (c) $\beta_i = 1.0$

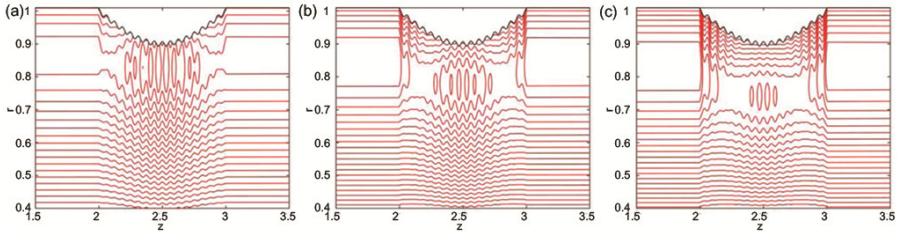

Fig. 16 — Streamlines for (a) $\alpha = 0$, (b) $\alpha = \frac{\pi}{4}$; and (c) $\alpha = \frac{\pi}{2}$

Table 3 — Computational values of $\left(\frac{\partial w}{\partial r}\right)_{r=1}$, $\left(\frac{\partial \theta}{\partial r}\right)_{r=1}$, and $\left(\frac{\partial \Phi}{\partial r}\right)_{r=1}$ for various values of controlling parameters

λ_1	c	β_e	β_i	α	θ_t	Ec	ϕ	γ_3	γ_4	MoS_2 - Blood			Au-MoS_2-Blood			MgO-Au-MoS_2-Blood		
										$-\left(\frac{\partial w}{\partial r}\right)_{r=1}$	$-\left(\frac{\partial \theta}{\partial r}\right)_{r=1}$	$-\left(\frac{\partial \Phi}{\partial r}\right)_{r=1}$	$-\left(\frac{\partial w}{\partial r}\right)_{r=1}$	$-\left(\frac{\partial \theta}{\partial r}\right)_{r=1}$	$-\left(\frac{\partial \Phi}{\partial r}\right)_{r=1}$	$-\left(\frac{\partial w}{\partial r}\right)_{r=1}$	$-\left(\frac{\partial \theta}{\partial r}\right)_{r=1}$	$-\left(\frac{\partial \Phi}{\partial r}\right)_{r=1}$
0.0	5	0.5	0.5	$\frac{\pi}{4}$	-2	1	5	0.1	0.1	5.6285	2.0667	0.8592	6.0044	2.0525	0.8878	6.0241	1.9250	0.9336
0.2										6.5985			7.0496			7.0739		
0.4										7.5692			8.0951			8.1243		
0.2	15									6.5553			7.0063			7.0306		
	25									6.5120			6.9631			6.9874		
	5	0.0								6.5539	2.7943		7.0051	2.7764		7.0344	2.5920	
		1.0								6.6313	1.5945		7.0823	1.5835		7.1028	1.5004	
		0.5	0.0							6.5827	2.4894		7.0337	2.4728		7.0598	2.3105	
			1.0							6.6114	1.7804		7.0624	1.7681		7.0852	1.6668	
		0.5	0							3.2059	2.0667		3.0802	2.0525		2.9131	1.9250	
				$\frac{\pi}{2}$						8.0038			8.6937			8.7973		
				$\frac{\pi}{4}$	-10					6.5985	2.2230		7.0496	2.2050		7.0739	2.0505	
					-6						2.2007			2.1834			2.0330	
					-2	2					2.9412			2.9226			2.7286	
						3					3.6209			3.6000			3.3691	
						1	1				2.0667	0.4193		2.0525	0.4250		1.9250	0.4342
							9					1.2991			1.3505			1.4330
							5	0.0		6.1728	2.4238	0.8592	6.5514	2.4053	0.8878	6.5517	2.2438	0.9336
								0.2		6.9337	1.7978		7.4417	1.7867		7.4849	1.6824	
								0.1	0.5	7.6148	2.0667	0.5859	8.2385	2.0525	0.6093	8.3202	1.9250	0.6471
									0.9	8.1353		0.3732	8.8475		0.3891	8.9585		0.4148

Nusselt number enhances for rising values of $\beta_e, \beta_i, \theta_t$ and γ_3, whereas it diminishes for Ec for mono, di and tri-hybrid nanofluids. The Sherwood number escalates for increasing value of γ_3 and de-escalates for ϕ for all three nanofluids. A comparative analysis of the axial velocity $w(r,z)$ across varying radial positions

Table 4 — Comparison for the values of $w(r,z)$ with previously published work at $\delta = 0.3, z = 3, d = 2, k_0 \to \infty, Gr = 4, \alpha = \frac{\pi}{4}, \theta_t = 1, S = 2, \lambda_1 = M = Gc = k^* = \delta^* = \varphi_{MoS_2} = \varphi_{Au} = \varphi_{MgO} = 0$

r	Nadeem and Ijaz[35]	Present study
0.2	0.0550	0.053201
0.4	0.0428	0.045182
0.6	0.0254	0.028413
0.8	0.0075	0.007105

(r) at $\delta = 0.3, z = 3, d = 2, k_0 \to \infty, Gr = 4, \alpha = \frac{\pi}{4}, \theta_t = 1, S = 2, \lambda_1 = M = Gc = k^* = \delta^* = \varphi_{MoS_2} = \varphi_{Au} = \varphi_{MgO} = 0$ with previously published work is presented in Table 4.

4 Conclusion

The hemodynamic behavior of a ternary hybrid Jeffery nanofluid in an inclined, uneven stenosed catheterized artery has been analyzed. The research highlights the roles of variable permeability and thermal conductivity, chemical reaction and Ohmic heating in modulating the flow rates. The significant observations derived from this study include

i Both Hall and ion-slip parameters significantly accelerate the axial velocity while simultaneously suppressing the entropy generation rate, demonstrating that these electromagnetic effects serve to accelerate the flow.

ii The skin friction coefficient undergoes a notable decline with the artery's inclination and Jeffery parameter. However, enhanced permeability of the arterial medium acts to improve the skin friction, reflecting a higher resistance at the vascular interface.

iii Temperature and entropy generation rise with an increase in the thermal conductivity parameter and Eckert number, underscoring the dominant influence of viscous dissipation and variable thermal properties on temperature distribution.

iv Tri-hybrid nanofluid demonstrates superior thermal regulation, maintaining lower temperature profiles compared to mono and di-hybrid counterparts. This highlights the increased heat-carrying capacity and efficiency afforded by the integration of ternary nanoparticles.

v Nusselt number and Sherwood number at the vascular wall are enhanced by rising thermal slip and concentration slip parameters, respectively.

vi Concentration profiles are suppressed by the concentration slip parameter but are markedly elevated by the chemical reaction parameter, indicating the role of reactive species in modulating the concentration field within the stenosed region.

vii The trapping improves for variable permeability and Hall parameters.

Future investigations could extend this theoretical framework by integrating fluid–structure interaction to account for elastic arterial wall deformability under realistic time-dependent pulsatile blood flow and incorporating patient-specific stenotic geometries reconstructed from clinical imaging. Furthermore, applying machine learning algorithms to optimize nanoparticle volume fractions and electromagnetic parameters could maximize localized hyperthermic efficiency while minimizing hemodynamic resistance.

Acknowledgement

The lead author gratefully recognizes the financial assistance received from the University Grants Commission (UGC), New Delhi, under the NTA Reference No. 211610058438.

References

1 Hayat T & Nawaz M, *Int J Numer Methods Fluids*, 66 (2011) 183.
2 Zhao X & Zhu M, *Z Angew Math Phys*, 68 (2018) 1.
3 Javed M & Naz R, *Waves Random Complex Medium*, 35 (2023) 5453.
4 Nowar K & Halouani B, *AIP Adv*, 15 (2025) 1.
5 Sheikh M, Almubaddel F S, Abdullaeva B, Bouzgarrou S M, Alam M M, Shahzadi R & Hasnain J, *Tribol Int*, 214 (2026) 1.
6 Choi S U S & Eastman J A, *Mater Sci*, 231 (1995) 99.
7 Ghadikolaei S S, Yassari M, Sadeghi H, Hosseinzadeh K & Ganji D D, *Powder Technol*, 322 (2017) 428.
8 Karthikeyan S, Ali F, Loganathan K & Thamaraikannan N, *J Taibah Univ Sci*, 18 (2024) 1.
9 Deshwal J, Chaudhary S & Kumar R, *Phys Scr*, 100 (2025) 1.
10 Kenea G & Ibrahim W, *Sci Rep*, 16 (2026) 1.
11 Prakash J, Ansu A K & Tripathi D, *Meccanica*, 53 (2018) 3719.
12 Ashraf M B, Rafiullah, Tanveer A & Ulhaq S, *J Magn Magn Mater*, 565 (2023) 1.
13 Vaidya H, Choudhari R V, Prasad K V & Naganur M, *Phys Fluids*, 36 (2024) 1.
14 Akolade M T, Agunbiade S A, Oyekunle T L & Malgwi P B, *Electrophoresis*, 46 (2025) 34.
15 Mujahid M, Areshi M, Abbas Z, Rafiq M Y & Elseesy I E, *Dyn Atmos Oceans*, 113 (2026) 1.
16 Tlau L & Ontela S, *Indian J Phys*, 95 (2021) 2095.
17 Santos-Moreno M, Valencia-Negrete C V& Fernandez-Anaya G, *Fractals*, 30 (2022) 1.
18 Hussain M, Farooq U & Sheremet M, *Numer Heat Transfer, Part B*, 86 (2023) 623.
19 Lone S A, Bossly R, Alduais F S, Al-Bossly A, Khan A & Saeed A, *Chin Phys B*, 34 (2025) 1.
20 Farooq J, Abbas A, Alshammari B M, Mir A & Kolsi L, *Alexandria Eng J*, 114 (2025) 426.

21 Rafaqat R & Khan A A, *Adv Mech Eng*, 13 (2021) 1.
22 El-Sapa S, Lotfy K, El-Bary A A & Ahmed M H, *Adv Condens Matter Phys*, 2023 (2023) 1.
23 Sheokand P, Deswal S & Punia B S, *J Therm Stresses*, 47 (2024) 217.
24 Mahanta C & Sharma R P, *J Therm Anal Calorim*, 150 (2025) 649.
25 Khan M, Imran M & Anwar M S, *Ain Shams Eng J*, 17 (2026) 1.
26 Sharma M K, Singh K & Bansal S, *J Biomed Sci Eng*,**7** (2014) 194.
27 Zaman A, Ali N & Sajid M, *AIP Adv*, 6 (2016) 1.
28 Tripathi J, Vasu B, Bég O A, Gorla R S R& Kameswaran P K, *Comput Biol Med*, 139 (2021) 1.
29 Dolui S, Bhaumik B & De S, *Chem Phys Lett*, 811 (2023) 1.
30 Changdar S & De S, *Iran J Sci Technol Trans A: Sci*, 43 (2019) 1259.
31 Roy A K & Bég O A, *Appl Math Comput*, 410 (2021) 1.
32 Basha H T, Rajagopal K, Ahammad N A, Sathish S & Gunakala S R, *Complexity*, 2022 (2022) 1.
33 Raju C S K, Basha H T, Noor N F M, Shah N A & Yook S J, *Math Comput Simul*, 215 (2024) 399.
34 Glili I E, Saidi A, Foukhari Y, Driouich M, Sammouda M& Gueraoui K, *J Comput Appl Mech*, 56 (2025) 87.
35 Nadeem S & Ijaz S, *Int J Heat Mass Transfer*, 93 (2016) 1137.